

Cite as: Z. Jia et al., Science 10.1126/science.adi0685 (2023).

The complex dynamics of the 2023 Kahramanmaraş, Turkey, $M_{\rm w}$ 7.8-7.7 earthquake doublet

Zhe Jia^{1*}, Zeyu Jin¹, Mathilde Marchandon², Thomas Ulrich², Alice-Agnes Gabriel^{1,2}, Wenyuan Fan¹, Peter Shearer¹, Xiaoyu Zou¹, John Rekoske¹, Fatih Bulut³, Asli Garagon³, Yuri Fialko¹

1Scripps Institution of Oceanography, UC San Diego, La Jolla, CA 92093, USA. 2Department of Earth and Environmental Sciences, Ludwig-Maximilians-Universit "at München, Munich, 80539, Germany, ³Geodesy Department, Bogazici University Kandilli Observatory and Earthquake Research Institute, Istanbul, 34342, Turkey.

*Corresponding author. Email: z5jia@ucsd.edu

The destructive 2023 moment magnitude (M_w) 7.8-7.7 earthquake doublet ruptured multiple segments of the East Anatolian Fault system in Turkey. We integrate multi-scale seismic and space-geodetic observations with multi-fault kinematic inversions and dynamic rupture modeling to unravel the events' complex rupture history and stress-mediated fault interactions. Our analysis reveals three sub-shear slip episodes during the initial M_w 7.8 earthquake with delayed rupture initiation to the southwest. The M_w 7.7 event occurred 9 hours later with larger slip and supershear rupture on its western branch. Mechanically consistent dynamic models accounting for fault interactions can explain the unexpected rupture paths, and require a heterogeneous background stress. Our results highlight the importance of combining near- and far-field observations with data-driven and physics-based models for seismic hazard assessment.

The moment magnitude (M_w) 7.8 and 7.7 Kahramanmaraş earthquakes in Turkey on February 6, 2023, caused enormous destruction and tens of thousands of casualties from collapsed structures, and were one of the deadliest natural disasters for Turkey and Syria over the last millennium (1). The Kahramanmaras sequence is the first great earthquake doublet with a combined moment magnitude of 8 recorded in a continental strike-slip fault system. Unlike regular aftershocks that are over one order of magnitude smaller than their mainshock, doublet events pose a greater hazard as they can cause more severe damage by striking already weakened buildings and structures. We show that the Kahramanmaras earthquake doublet involved a remarkable sequence of subevents that occurred with varying rupture velocities, geometries, and time delays on branched fault segments, which challenge our understanding of earthquake interactions and the dynamics of rupture propagation.

Seismologists commonly approximate earthquakes as point sources or as slip along a single fault with fixed rupture velocity. However, large earthquakes often rupture multiple fault segments within a complex network (2–6). Occasionally, events of a comparable magnitude occur within minutes to hours of the initial event, resulting in earthquake doublets (7-9). Branching faults may further complicate rupture dynamics (10-12). Whether rupture stops or continues propagating at fault junctions can determine earthquakes' eventual size and destructive potential (13). When applied to complex ruptures on multiple faults, conventional earthquake source imaging often involves oversimplified assumptions, vielding stark differences in source models and their interpretations

First release: 3 August 2023

(14. 15). Initial studies of the Kahramanmaraş earthquakes presented a wide range of earthquake models and interpretations (16-21), likely due to focusing on particular datasets and aspects of the rupture process. These differences motivate unified and self-consistent approaches that integrate diverse datasets with state-of-the-art rupture models to advance our understanding of the earthquake dynamics.

We perform a comprehensive investigation of the $M_{\rm w}$ 7.8-7.7 Kahramanmaras doublet using data-driven and physicsbased analyses applied to near- and far-field seismic and geodetic observations. Our results reveal that the earthquakes followed unexpected rupture trajectories, which included delayed backward branching, statically- and dynamically aided triggering, and a combination of subshear and supershear rupture episodes. These discoveries call for reevaluating the role of cascading failure mechanisms when assessing the destructive potential of large earthquakes within complex fault networks.

The geometrically complex $M_{\rm w}$ 7.8-7.7 earthquake doublet

On Feb 6, 2023, two major (moment magnitude greater than 7) earthquakes ruptured several previously recognized fault systems within nine hours (Fig. 1). The EAF is a mature transform fault accommodating up to 10 mm/y of left-lateral motion between the Arabian and Anatolian plates (22) (Fig. 1). Several $M_{\rm w}$ ~7 earthquakes occurred on the EAF historically, but none ruptured the entire southern section of the EAF (23). The estimated dimensions of the historic events suggest that geometric complexities such as fault bends and step-overs may have controlled the event sizes (23, 24). The second earthquake $(M_{\rm w}$ 7.7) occurred on the Savrun-Çardak Fault (SCF), extending ~150 km along the east-west direction (Fig. 1). The SCF has been relatively quiescent, with only two moderate $(M_{\rm w}$ <6) events recorded in the past 100 years (25).

We constrain the rupture geometry based on surface traces mapped using Synthetic Aperture Radar data (26) and precisely relocated aftershocks (27, 28). We find that the Kahramanmaraş doublet ruptured at least six major fault segments (Fig. 1). The epicenter of the $M_{\rm w}$ 7.8 earthquake is located on a subsidiary fault, the Nurdağı-Pazarcık Fault (NPF, fault 1 in Fig. 1A) (20), from which the rupture propagated to the EAF, and then ruptured along the EAF to both the northeast and southwest (faults 2 and 3), for a total length of about 300 km. Unlike the historical M~7 events, the $M_{\rm w}$ 7.8 earthquake propagated across at least four possible geometric barriers, including fault bends and stepovers.

The static slip distribution (Fig. 1B) obtained from inversions of Synthetic Aperture Radar (SAR) and Global Navigation Satellite System (GNSS) data (figs. S1 to S7) shows that the largest slip in the $M_{\rm w}$ 7.8 event is on the EAF at its junction with the NPF, near the towns of Kahramanmaraş and Pazarcik, with peak slip in excess of 8 m. Most of the coseismic slip is in the upper 20 km of the seismogenic layer (Fig. 1B). Slip at the surface is highly heterogeneous, consistent with field observations (18), but on average increasing from the southwest to the northeast ends of the $M_{\rm w}$ 7.8 rupture (fig. S8). The area of substantial slip extends to the northeast from the junction for about 150 km to the western tip of the 2020 $M_{\rm w}$ 6.7 Elazig rupture (29) (Fig. 1A). South of the junction, the $M_{\rm w}$ 7.8 rupture extends to the southern end of the EAF. The average coseismic slip on the southwest branch of the $M_{\rm w}$ 7.8 rupture is smaller than the average slip on the northeast branch (Fig. 1B and fig. S2).

We resolve the spatiotemporal rupture process with a subevent inversion method using both near- and far-field seismic observations (30, 31). The $M_{\rm w}$ 7.8 earthquake has six subevents altogether spanning ~90 s (Fig. 2A). The $M_{\rm w}$ 6.8 subevent E1 that ruptures the NPF is followed 18 s later by the largest subevent E2 ($M_{\rm w}$ 7.5) at the NPF-EAF intersection. The earthquake then ruptured northeastward along the EAF for about 130 km ($M_{\rm w}$ 7.5 subevent E3), as well as, after a short delay, backward from the NPF junction for about 150 km along the southwestern segment of the EAF, with integrated slip equivalent to a $M_{\rm w}$ 7.4 earthquake (subevents E4-E6). Teleseismic P-wave back-projection (32) confirms the rupture process with imaged high-frequency radiation peaks outlining the major subevents (Fig. 2A) and indicating an average rupture velocity of 3 km/s. To further constrain the slip history, we perform a joint kinematic slip inversion of the $M_{\rm w}$ 7.8 earthquake constrained by far- and near-field seismic and geodetic data (26, 33). Our kinematic inversion results agree

First release: 3 August 2023

with the static and subevent models (Fig. 2B). The best-fit kinematic slip model images 10-s-delayed backward branching at the NPF-EAF intersection, toward the southwest (Fig. 2B), constrained by the strong-motion data (fig. S17). It also indicates average rupture velocities of 3.2 km/s and 2.8 km/s for the northeastern and southwestern branches, respectively (fig. S18). Tracking ground motion pulses at near-fault strong motion stations along the southwestern segment, also yields a rupture velocity of \sim 3 km/s (fig. S18), confirming an overall subshear nature. All our kinematic models consistently reveal a \sim 300 km-long complex bilateral multi-segment rupture, subshear rupture velocities, and delayed triggering of the southwest segment of the $M_{\rm w}$ 7.8 event (Fig. 2C).

The subsequent $M_{\rm w}$ 7.7 earthquake ruptured a 150-km long section of the west-trending SCF, within 90 km of the $M_{\rm w}$ 7.8 earthquake hypocenter. The aftershock distribution and surface offsets indicate branching and abrupt changes in strike at both the eastern and western ends of the $M_{\rm w}$ 7.7 rupture (Fig. 1). Geodetic data and our associated static slip model (Fig. 1B) suggest rupture along an 80-km-long segment of the SCF system (fault 4-5 in Fig. 1), but not along the eastern end of the Sürgü fault that connects to the EAF. Instead, the $M_{\rm w}$ 7.7 rupture diverted sharply onto the Doğanşehir branch, which angles to the northeast (fault 6). The $M_{\rm w}$ 7.7 event shows a concentrated slip distribution with over 10 m peak slip around its hypocenter, suggesting a substantially higher stress drop than the initial $M_{\rm w}$ 7.8 earthquake which spreads lower-amplitude slip over a larger region.

Our analysis of the rupture history of the $M_{\rm w}$ 7.7 event identifies four major subevents, lasting for about 30 s (Fig. 3A). The first three subevents, E1-E3, all cluster near the epicenter and account for over 80% of the total seismic moment, suggesting a compact bilateral rupture in the central SCF. The focal mechanism (strike of 237°) and location of the last subevent (E4, $M_{\rm w}$ 7.1) agree with the static slip model on the Doğansehir branch (Fig. 1B). All subevents of both earthquakes have almost pure double-couple mechanisms (Figs. 2A and 3A), suggesting that the strong non-double couple components in the Global Centroid-Moment-Tensor solutions (34) (Fig. 1A) are due to highly variable rupture geometries. The overall shorter duration and smaller rupture extent of the $M_{\rm w}$ 7.7 event make back-projection analysis less effective for resolving rupture details, but our kinematic finite-slip inversion can still be applied.

The kinematic finite-fault model of the $M_{\rm w}$ 7.7 earthquake also indicates a compact slip distribution. In addition, it indicates a westward rupture velocity of approximately 4.5 km/s (Fig. 3B), exceeding the shear-wave speed in the crust. The waveforms recorded at the westward seismic stations strongly constrain this supershear rupture episode (Fig. 3C and fig. S19), which is consistent with analysis of high-rate GNSS data (20). In contrast, the eastward rupture likely

propagated at a slower velocity of 2.5 km/s. The intriguing supershear rupture episode may imply locally higher prestress (35) and high stress drop (36) as in our dynamic rupture models.

Dynamics, triggering, and stress interaction of the doublet

Dynamic rupture modeling involves simulating how earthquakes nucleate, propagate, and arrest. Unlike purely data-driven kinematic slip inversions, such models predict the evolution of slip, seismic waves, and surface deformation in a physically self-consistent manner. Detailed, physics-based interpretations can help verify whether inferred rupture scenarios are mechanically plausible, but are computationally challenging and typically take years to develop (e.g., 10.12.13).

We present data-informed dynamic rupture simulations of the 2023 Kahramanmaraş earthquakes that illuminate complex details of the rupture process. Our 3D dynamic rupture models include stress changes computed from the slip distribution of the static slip model (37), large-scale variability in fault loading inferred from regional seismo-tectonics, and the relative effects of the static and dynamic stresses of the $M_{\rm w}$ 7.8 event on the faults hosting the second earthquake (26) (fig. S20). The dynamic rupture models independently reproduce the main features of the kinematic models (Fig. 4 and fig. S21), providing a physics-based validation of the inferred rupture histories.

Our forward simulations use the complex fault geometries of both earthquakes informed from geodetic analysis (Fig. 1) to spontaneously replicate the moment rate release, magnitude, rupture velocity and delays, as well as the lack of instantaneous dynamic triggering of the $M_{\rm w}$ 7.7 event. The dynamic rupture synthetics produce surface displacements and slip histories that compare well to the high-resolution geodetic data (fig. S22), kinematic rupture representations (Fig. 4 and fig. S21) and observed ground motions (Fig. 5 and figs. S23 to S25). Figure 4A illustrates the modeled $M_{\rm w}$ 7.8 earthquake dynamics. The NPF-EAF intersection slows sub-shear rupture on the NPF which then branches with dynamically favorable forward directivity (38) northeastward along the EAF. The large fault branching angle poses a strong dynamic barrier in backward-directivity (39) leading to significantly delayed EAF rupture toward the southwest. Continuous dynamic unclamping, transient shear stressing and static stress build-up at the fault intersection due to the unilaterally propagating northeast rupture allows the rupture to eventually fracture the EAF bilaterally (fig. S26). Rupture speed remains overall sub-shear during the earthquake (Fig. 4B).

Dynamic rupture modeling of the $M_{\rm w}$ 7.7 earthquake features bi-lateral rupture with unequal rupture speeds, confirming dominant supershear westward and sub-shear

First release: 3 August 2023

eastward propagation. Our $M_{\rm w}$ 7.8 dynamic rupture model predicts a highly variable pattern of static and dynamic stresses resolved on the faults that hosted the $M_{\rm w}$ 7.7 earthquake (Fig. 4, C and D). The hypocentral area of the $M_{\rm w}$ 7.7 event experienced an increase in static Coulomb stress of several hundred kilopascals due to the $M_{\rm w}$ 7.8 earthquake, resulting from both an increase in shear stress and a decrease in fault-normal compression (fig. S27). It also experienced a much larger transient increase in the Coulomb stress of a few megapascals due to passing seismic waves (Fig. 4D), which nevertheless did not result in instantaneous triggering.

Discussion and Conclusions

Our analyses reveal unexpected rupture paths. The Kahramanmaraş doublet originated as a moderate event on the NPF branch fault with a magnitude of only 6.8, yet the rupture was able to successfully cross the junction of the NPF and EAF, which would usually be considered a geometric barrier that conditionally gates the rupture propagation (40, 41). As a result, the earthquake intensified with the northeastward propagation along the EAF, then dynamically triggered backward rupture toward the southwest by continuously unclamping and stressing from the forward branch, eventually culminating in a $M_{\rm w}$ 7.8 event, with total seismic moment increased by a factor of 30 compared to the initial rupture on the NPF. In addition, the $M_{\rm w}$ 7.8 earthquake increased the Coulomb stress on the central part of the SCF, which may have aided the nucleation of the $M_{\rm w}$ 7.7 earthquake 9 hours later. The entire process highlights the additional hazard brought by rupture triggering across a network of faults, challenging earthquake hazard assessments that typically do not consider such multi-fault triggering scenarios.

The $M_{\rm w}$ 7.8 earthquake involved backward fault branching, which is highly unfavorable from a dynamic perspective, thus commonly neglected in hazard studies. Several previous continental earthquakes, including the 1992 Landers, the 1999 Hector Mine, and the 2002 Denali earthquakes, have also exhibited localized backward branching (10). Existing explanations of this phenomenon include backward rupture jumping induced by sudden rupture arresting or nonuniform prestress fields caused by earthquake cycles (39, 42). Our dynamic rupture models indicate that backward branching during the $M_{\rm w}$ 7.8 event does not necessarily require a complex arrangement of the receiver fault (42) or triggering of supershear rupture (43). Instead, the progressive build-up of slip on the forward branch of the EAF continuously unclamps and stresses the backward branch of the EAF, eventually leading to delayed and self-sustained branching toward the southwest, which is a simple yet effective mechanism.

One of the surprising aspects of the $M_{\rm w}$ 7.7 earthquake is that it did not rupture through the eastern Sürgü segment and arrive at the EAF, contrary to earlier suggestions (20),

but instead deviated to the Doğanşehir branch. The InSAR, aftershock, and seismic data clearly show such a deviation (figs. S1 and S14). The straightforward rupture path along the Sürgü fault was encouraged by the static stress changes due to the $M_{\rm w}$ 7.8 event (fig. S27), unlike the sharp deviation to the Doğanşehir fault which was actually unloaded by the $M_{\rm w}$ 7.8 event (Fig. 4D and movie S3). Possible explanations, which may be tested by future geodetic and seismological observations, include velocity-strengthening behavior of the eastern Sürgü segment, or local stress heterogeneity, e.g., due to past earthquakes (44). Considerable regional stress heterogeneity, as is required by our dynamic rupture models (fig. S20), is implied by extremely complex rupture geometries involving changes in the strike angle of up to 90 degrees (Fig. 1) Fig. and fig. S27) (45). Some faults in the study area, including the EAF, exhibit shallow creep (46), however creep has to be pervasive to potentially suppress an incoming dynamic rupture. Observations spanning all phases of the earthquake cycle are needed to constrain the velocity- and depth-dependent frictional properties of active faults (47, 48). Shallow creep might be responsible for a substantial reduction in the amplitude of coseismic slip in the top few kilometers of the upper crust (Fig. 1B), which is well resolved in our inverse models (fig. S28). Subsequent observations will show whether this reduction can be compensated by shallow afterslip or constitutes a long-term shallow slip deficit (49), implying wide-spread off-fault yielding (47, 50).

We also find intriguing variations in rupture velocity across segments of the EAF-SCF fault network. Although the $M_{\rm w}$ 7.8 event produced extreme shaking with peak ground accelerations (PGA) exceeding 1 g for near-fault stations, the observed and simulated $M_{\rm w}$ 7.7 ground motions are similar or larger when compared at the same distance (Fig. 5 and figs. S23 and S24), consistent with a potentially larger stress drop of the $M_{\rm w}$ 7.7 event. The modeled and observed $M_{\rm w}$ 7.7 event shaking shows less distance dependence, which may be due to the effects of supershear rupture.

The western branch of the SCF experienced a supershear rupture episode, while the eastern SCF branch and the EAF hosted subshear ruptures with considerable delays. In general, our modeling shows that the pre-event stress heterogeneities, dynamic and static redistribution of stress and the geometry of the faults may control these diverse rupture characteristics.

The Kahramanmaras doublet ruptured multiple faults in distinct slip episodes, likely involving complex stress-triggering processes across different temporal and spatial scales. Such processes resulted in the increased rupture length and seismic moment of the Turkey earthquake doublet, and a substantially larger destructive potential compared with the "typical" $M_{\rm w}$ ~7 historical earthquakes in the region (23). Such a variability might be interpreted in terms of the super-

First release: 3 August 2023

cycle model (51). By using integrated methods that combine near- and far-field seismic and geodetic observations and investigating data-derived models and physics-based rupture simulations, we show that stress interactions, and static and dynamic triggering worked together across a complex fault system, resulting in a cascade of rupture with a larger than usual total rupture length and moment magnitude. Our study shows that complementary data-driven and physics-based analyses, which in isolation often lead to non-unique or even contradictory results, can jointly and efficiently unravel highly complex earthquake dynamics based on dense nearfield observations. The unusual static and dynamic interactions during and between the events of the Kahramanmaras doublet call for reassessment of common assumptions built into seismic hazard assessments.

REFERENCES AND NOTES

- 1. M. Edrik, M. B. D. Tümsa, A. Pınar, E. Altunel, A. C. Zülfikar, "A preliminary report on the February 6, 2023 earthquakes in Türkiye" (Temblor, 2023)
- 2. T. Lay, L. Ye, Y. Bai, K. F. Cheung, H. Kanamori, The 2018 MW 7.9 Gulf of Alaska earthquake: Multiple fault rupture in the Pacific plate. Geophys. Res. Lett. 45. 9542-9551 (2018). doi:10.1029/2018GL079813
- 3. L. Meng, J.-P. Ampuero, J. Stock, Z. Duputel, Y. Luo, V. C. Tsai, Earthquake in a maze: Compressional rupture branching during the 2012 M(w) 8.6 Sumatra earthquake. Science 337, 724–726 (2012). doi:10.1126/science.1224030 Medline
- 4. E. Hauksson, L. M. Jones, K. Hutton, The 1999 M w 7.1 Hector Mine, California, earthquake sequence: Complex conjugate strike-slip faulting. Bull. Seismol. Soc. Am. 92, 1154-1170 (2002). doi:10.1785/0120000920
- E. Hauksson, L. M. Jones, K. Hutton, D. Eberhart-Phillips, The 1992 Landers earthquake sequence: Seismological observations. J. Geophys. Res. 98 (B11), 19835-19858 (1993). doi:10.1029/93JB02384
- 6. Z. E. Ross, B. Idini, Z. Jia, O. L. Stephenson, M. Zhong, X. Wang, Z. Zhan, M. Simons, E. J. Fielding, S.-H. Yun, E. Hauksson, A. W. Moore, Z. Liu, J. Jung, Hierarchical interlocked orthogonal faulting in the 2019 Ridgecrest earthquake sequence. Science 366, 346-351 (2019). doi:10.1126/science.aaz0109 Medline
- 7. A. Ghods, E. Shabanian, E. Bergman, M. Faridi, S. Donner, G. Mortezanejad, A. Aziz-Zanjani, The Varzaghan-Ahar, Iran, Earthquake Doublet (M w 6.4, 6.2): Implications for the geodynamics of northwest Iran. Geophys. J. Int. 203, 522-540 (2015). doi:10.1093/gji/ggv306
- 8. C. J. Ammon, H. Kanamori, T. Lay, A great earthquake doublet and seismic stress transfer cycle in the central Kuril islands. Nature 451, 561-565 (2008). doi:10.1038/nature06521 Medline
- W. Fan, P. M. Shearer, Local near instantaneously dynamically triggered aftershocks of large earthquakes. Science **353**, 1133–1136 (2016).doi:10.1126/science.aag0013 Medline
- 10. D. D. Oglesby, S. M. Day, Y.-G. Li, J. E. Vidale, The 1999 Hector Mine earthquake: The dynamics of a branched fault system. Bull. Seismol. Soc. Am. 93, 2459–2476 (2003). doi:10.1785/0120030026
- 11. H. S. Bhat, M. Olives, R. Dmowska, J. R. Rice, Role of fault branches in earthquake rupture dynamics. J. Geophys. Res. 112 (B11), B11309 (2007).doi:10.1029/2007JB005027
- 12. T. Ulrich, A.-A. Gabriel, J.-P. Ampuero, W. Xu, Dynamic viability of the 2016 Mw 7.8 Kaikōura earthquake cascade on weak crustal faults. Nat. Commun. 10, 1213 (2019). doi:10.1038/s41467-019-09125-w Medline
- 13. R. Douilly, H. Aochi, E. Calais, A. Freed, Three-dimensional dynamic rupture simulations across interacting faults: The Mw7. 0, 2010, Haiti earthquake. J. Geophys. Res. Solid Earth 120, 1108-1128 (2015). doi:10.1002/2014JB011595
- 14. S. Minson, M. Simons, J. Beck, Bayesian inversion for finite fault earthquake source models I-Theory and algorithm. Geophys. J. Int. 194, 1701-1726 (2013). doi:10.1093/gii/ggt180

science.org

- K. Wang, D. S. Dreger, E. Tinti, R. Bürgmann, T. Taira, Rupture process of the 2019 Ridgecrest, California M w 6.4 foreshock and M w 7.1 earthquake constrained by seismic and geodetic data. *Bull. Seismol. Soc. Am.* 110, 1603–1626 (2020). doi:10.1785/0120200108
- S. Barbot, H. Luo, T. Wang, Y. Hamiel, O. Piatibratova, M. T. Javed, C. Braitenberg,
 G. Gurbuz, Slip distribution of the February 6, 2023 Mw 7.8 and Mw 7.6,
 Kahramanmaraş, Turkey earthquake sequence in the East Anatolian Fault Zone.
 Seismica 2, (2023). doi:10.26443/seismica.v2i3.502
- 17. D. E. Goldberg, T. Taymaz, N. G. Reitman, A. E. Hatem, S. Yolsal-Çevikbilen, W. D. Barnhart, T. S. Irmak, D. J. Wald, T. Öcalan, W. L. Yeck, B. Özkan, J. A. Thompson Jobe, D. R. Shelly, E. M. Thompson, C. B. DuRoss, P. S. Earle, R. W. Briggs, H. Benz, C. Erman, A. H. Doğan, C. Altuntaş, Rapid Characterization of the February 2023 Kahramanmaraş, Türkiye, Earthquake Sequence. Seismic Record 3, 156–167 (2023). doi:10.1785/0320230009
- V. Karabacak, Ç. Özkaymak, H. Sözbilir, O. Tatar, B. Aktuğ, Ö. C. Özdağ, R. Çakir, E. Aksoy, F. Koçbulut, M. Softa, E. Akgün, A. Demir, G. Arslan, The 2023 Pazarcık (Kahramanmaraş, Türkiye) earthquake (M_w 7.7): Implications for surface rupture dynamics along the East Anatolian Fault Zone. *J. Geol. Soc. London* 180, jgs2023– jgs2020 (2023). doi:10.1144/jgs2023-020
- P. M. Mai, T. Aspiotis, T. A. Aquib, E. V. Cano, D. Castro-Cruz, A. Espindola-Carmona, B. Li, X. Li, J. Liu, R. Matrau, A. Nobile, K. H. Palgunadi, M. Ribot, L. Parisi, C. Suhendi, Y. Tang, B. Yalcin, U. Avşar, Y. Klinger, S. Jónsson, The Destructive Earthquake Doublet of 6 February 2023 in South-Central Türkiye and Northwestern Syria: Initial Observations and Analyses. Seismic Record 3, 105–115 (2023). doi:10.1785/0320230007
- D. Melgar, T. Taymaz, A. Ganas, B. Crowell, T. Öcalan, M. Kahraman, V. Tsironi, S. Yolsal-Çevikbilen, S. Valkaniotis, T. S. Irmak, T. Eken, C. Erman, B. Özkan, A. H. Dogan, C. Altuntaş, Sub- and super-shear ruptures during the 2023 Mw 7.8 and Mw 7.6 earthquake doublet in SE Türkiye. Seismica 2, (2023). doi:10.26443/seismica.v2i3.387
- R. Okuwaki, Y. Yagi, T. Taymaz, S. P. Hicks, Multi-Scale Rupture Growth With Alternating Directions in a Complex Fault Network During the 2023 South-Eastern Türkiye and Syria Earthquake Doublet. *Geophys. Res. Lett.* 50, e2023GL103480 (2023). doi:10.1029/2023GL103480
- 22. N. Lyberis, T. Yurur, J. Chorowicz, E. Kasapoglu, N. Gundogdu, The East Anatolian Fault: An oblique collisional belt. *Tectonophysics* **204**, 1–15 (1992). doi:10.1016/0040-1951(92)90265-8
- S. E. Güvercin, H. Karabulut, A. Ö. Konca, U. Doğan, S. Ergintav, Active seismotectonics of the East Anatolian Fault. *Geophys. J. Int.* 230, 50–69 (2022). doi:10.1093/gji/ggac045
- T. Y. Duman, Ö. Emre, The East Anatolian Fault: Geometry, segmentation and jog characteristics. Spec. Publ. Geol. Soc. Lond. 372, 495–529 (2013). doi:10.1144/SP372.14
- A. Koç, N. Kaymakcı, Kinematics of Sürgü fault zone (Malatya, Turkey): A remote sensing study. J. Geodyn. 65, 292–307 (2013). doi:10.1016/j.jog.2012.08.001
- 26. Materials and methods are available as supplementary materials.
- 27. Z. Jin, Y. Fialko, Finite slip models of the 2019 Ridgecrest earthquake sequence constrained by space geodetic data and aftershock locations. *Bull. Seismol. Soc. Am.* **110**, 1660–1679 (2020). doi:10.1785/0120200060
- 28. A. Lomax, Precise, NLL-SSST-coherence hypocenter catalog for the 2023 M_w 7.8 and M_w 7.6 SE Turkey earthquake sequence, Zenodo (2023); https://10.5281/zenodo.7699881.
- 29. A. Doğru, F. Bulut, C. Yaltırak, B. Aktuğ, Slip distribution of the 2020 Elaziğ Earthquake (M w 6.75) and its influence on earthquake hazard in the Eastern Anatolia. *Geophys. J. Int.* **224**, 389–400 (2021). doi:10.1093/gji/ggaa471
- Z. Jia, Z. Shen, Z. Zhan, C. Li, Z. Peng, M. Gurnis, The 2018 Fiji Mw 8.2 and 7.9 deep earthquakes: One doublet in two slabs. *Earth Planet. Sci. Lett.* 531, 115997 (2020). doi:10.1016/j.epsl.2019.115997
- 31. Z. Jia, Z. Zhan, H. Kanamori, The 2021 south Sandwich Island Mw 8.2 Earthquake: A slow event sandwiched between regular ruptures. *Geophys. Res. Lett.* 49, e2021GL097104 (2022). doi:10.1029/2021GL097104
- 32. M. Ishii, P. M. Shearer, H. Houston, J. E. Vidale, Extent, duration and speed of the 2004 Sumatra-Andaman earthquake imaged by the Hi-Net array. *Nature* **435**, 933–936 (2005). doi:10.1038/nature03675 Medline

First release: 3 August 2023

- Z. Jia, X. Wang, Z. Zhan, Multifault models of the 2019 Ridgecrest sequence highlight complementary slip and fault junction instability. *Geophys. Res. Lett.* 47, e2020GL089802 (2020). doi:10.1029/2020GL089802
- G. Ekström, M. Nettles, A. Dziewoński, The global CMT project 2004–2010: Centroid-moment tensors for 13,017 earthquakes. *Phys. Earth Planet. Inter.* 200-201, 1–9 (2012). doi:10.1016/j.pepi.2012.04.002
- C. Liang, J. P. Ampuero, D. Pino Muñoz, The paucity of supershear earthquakes on large faults governed by rate and state friction. *Geophys. Res. Lett.* 49, e2022GL099749 (2022). doi:10.1029/2022GL099749
- 36. E. M. Dunham, Conditions governing the occurrence of supershear ruptures under slip-weakening friction. *J. Geophys. Res. Solid Earth* 112, JB004717 (2007).
- 37. E. Tinti, E. Casarotti, T. Ulrich, T. Taufiqurrahman, D. Li, A.-A. Gabriel, Constraining families of dynamic models using geological, geodetic and strong ground motion data: The Mw 6.5, October 30th, 2016, Norcia earthquake, Italy. *Earth Planet. Sci. Lett.* 576, 117237 (2021). doi:10.1016/j.epsl.2021.117237
- 38. N. Kame, J. R. Rice, R. Dmowska, Effects of prestress state and rupture velocity on dynamic fault branching. *J. Geophys. Res. Solid Earth* **108**, JB002189 (2003).
- 39. S. Fliss, H. S. Bhat, R. Dmowska, J. R. Rice, Fault branching and rupture directivity. *J. Geophys. Res. Solid Earth* **110**, JB003368 (2005).
- 40. G. King, J. Nabecaronlek, Role of fault bends in the initiation and termination of earthquake rupture. *Science* **228**, 984–987 (1985). doi:10.1126/science.228.4702.984 Medline
- D. Andrews, Mechanics of fault junctions. J. Geophys. Res. 94 (B7), 9389–9397 (1989). doi:10.1029/JB094iB07p09389
- 42. B. Duan, D. D. Oglesby, Nonuniform prestress from prior earthquakes and the effect on dynamics of branched fault systems. *J. Geophys. Res. Solid Earth* 112, JB004443 (2007).
- 43. A. Rosakis, M. Abdelmeguid, A. Elbanna, Evidence of Early Supershear Transition in the $M_{\rm w}$ 7.8 Kahramanmaraş Earthquake From Near-Field Records. arXiv:2302.07214, (2023).
- 44. S. S. Nalbant, J. McCloskey, S. Steacy, A. A. Barka, Stress accumulation and increased seismic risk in eastern Turkey. *Earth Planet. Sci. Lett.* **195**, 291–298 (2002). doi:10.1016/S0012-821X(01)00592-1
- 45. Y. Fialko, Estimation of absolute stress in the hypocentral region of the 2019 Ridgecrest, California, earthquakes. *J. Geophys. Res. Solid Earth* 126, e2021JB022000 (2021). doi:10.1029/2021JB022000
- Z. Cakir, U. Doğan, A. M. Akoğlu, S. Ergintav, S. Özarpacı, A. Özdemir, T. Nozadkhalil, N. Çakir, C. Zabcı, M. H. Erkoç, M. Basmenji, M. Köküm, R. Bilham, Arrest of the Mw 6.8 January 24, 2020 Elaziğ (Turkey) earthquake by shallow fault creep. Earth Planet. Sci. Lett. 608, 118085 (2023). doi:10.1016/j.epsl.2023.118085
- 47. Y. Kaneko, Y. Fialko, D. T. Sandwell, X. Tong, M. Furuya, Interseismic deformation and creep along the central section of the North Anatolian Fault (Turkey): InSAR observations and implications for rate-and-state friction properties. *J. Geophys. Res. Solid Earth* 118, 316–331 (2013). doi:10.1029/2012JB009661
- 48. E. O. Lindsey, Y. Fialko, Geodetic constraints on frictional properties and earthquake hazard in the Imperial Valley, Southern California. *J. Geophys. Res. Solid Earth* **121**, 1097–1113 (2016). doi:10.1002/2015JB012516
- 49. Y. Fialko, D. Sandwell, M. Simons, P. Rosen, Three-dimensional deformation caused by the Bam, Iran, earthquake and the origin of shallow slip deficit. *Nature* 435, 295–299 (2005). doi:10.1038/nature03425 Medline
- 50. Z. Jin, Y. Fialko, Coseismic and early postseismic deformation due to the 2021 M7. 4 Maduo (China) earthquake. Geophys. Res. Lett. 48, e2021GL095213 (2021). doi:10.1029/2021GL095213
- 51. L. Dal Zilio, J.-P. Ampuero, Earthquake doublet in Turkey and Syria. *Commun. Earth Environ.* **4**, 71 (2023). doi:10.1038/s43247-023-00747-z
- 52. L. Luzi, F. Pacor, G. Lanzano, C. Felicetta, R. Puglia, M. D'Amico, 2016–2017 Central Italy seismic sequence: Strong-motion data analysis and design earthquake selection for seismic microzonation purposes. *Bull. Earthquake Eng.* 18, 5533–5551 (2020). doi:10.1007/s10518-019-00676-3
- Disaster and Emergency Management Authority (AFAD), (1973); https://deprem.afad.gov.tr/event-catalog

- 54. T. Taufiqurrahman, A.-A. Gabriel, D. Li, T. Ulrich, B. Li, S. Carena, A. Verdecchia, F. Gallovič, Dynamics, interactions and delays of the 2019 Ridgecrest rupture sequence. *Nature* 618, 308–315 (2023). doi:10.1038/s41586-023-05985-x Medline
- S. Akkar, M. A. Sandıkkaya, J. J. Bommer, Empirical ground-motion models for point-and extended-source crustal earthquake scenarios in Europe and the Middle East. *Bull. Earthquake Eng.* 12, 359–387 (2014). doi:10.1007/s10518-013-9461-4
- D. Sandwell, R. Mellors, X. Tong, M. Wei, P. Wessel, GMTSAR: An InSAR processing system based on generic mapping tools (UC San Diego: Scripps Institution of Oceanography, 2011).
- 57. T. G. Farr, P. A. Rosen, E. Caro, R. Crippen, R. Duren, S. Hensley, M. Kobrick, M. Paller, E. Rodriguez, L. Roth, D. Seal, S. Shaffer, J. Shimada, J. Umland, M. Werner, M. Oskin, D. Burbank, D. Alsdorf, The shuttle radar topography mission. *Rev. Geophys.* 45, RG2004 (2007). doi:10.1029/2005RG000183
- R. M. Goldstein, H. A. Žebker, C. L. Werner, Satellite radar interferometry: Twodimensional phase unwrapping. *Radio Sci.* 23, 713–720 (1988). doi:10.1029/RS023i004p00713
- 59. T. A. Herring, T. I. Melbourne, M. H. Murray, M. A. Floyd, W. M. Szeliga, R. W. King, D. A. Phillips, C. M. Puskas, M. Santillan, L. Wang, Plate Boundary Observatory and related networks: GPS data analysis methods and geodetic products. *Rev. Geophys.* 54, 759–808 (2016). doi:10.1002/2016RG000529
- 60. J. Böhm, A. Niell, P. Tregoning, H. Schuh, Global Mapping Function (GMF): A new empirical mapping function based on numerical weather model data. *Geophys. Res. Lett.* **33**, L07304 (2006). doi:10.1029/2005GL025546
- F. Lyard, F. Lefevre, T. Letéllier, O. Francis, Modelling the global ocean tides: Modern insights from FES2004. Ocean Dyn. 56, 394–415 (2006). doi:10.1007/s10236-006-0086-x
- 62. D. D. McCarthy, G. Petit, "IERS conventions (2003)" (International Earth Rotation And Reference Systems Service (Iers)(Germany), 2004).
- K. Wang, Y. Fialko, Slip model of the 2015 Mw 7.8 Gorkha (Nepal) earthquake from inversions of ALOS-2 and GPS data. *Geophys. Res. Lett.* 42, 7452–7458 (2015). doi:10.1002/2015GL065201
- 64. Y. Fialko, Probing the mechanical properties of seismically active crust with space geodesy: Study of the coseismic deformation due to the 1992 Mw7. 3 Landers (southern California) earthquake. *J. Geophys. Res. Solid Earth* **109**, JB002756 (2004).
- 65. R. Wang, F. L. Martín, F. Roth, Computation of deformation induced by earthquakes in a multi-layered elastic crust—FORTRAN programs EDGRN/EDCMP. Comput. Geosci. 29, 195–207 (2003). doi:10.1016/S0098-3004(02)00111-5
- T. Bodin, M. Sambridge, H. Tkalčić, P. Arroucau, K. Gallagher, N. Rawlinson, Transdimensional inversion of receiver functions and surface wave dispersion. *J. Geophys. Res. Solid Earth* 117, JB008560 (2012).
- S. E. Minson, D. S. Dreger, Stable inversions for complete moment tensors. Geophys. J. Int. 174, 585–592 (2008). doi:10.1111/j.1365-246X.2008.03797.x
- B. Kennett, E. Engdahl, Traveltimes for global earthquake location and phase identification. Geophys. J. Int. 105, 429–465 (1991). doi:10.1111/j.1365-246X.1991.tb06724.x
- M. Kikuchi, H. Kanamori, Inversion of complex body waves—III. Bull. Seismol. Soc. Am. 81, 2335–2350 (1991). doi:10.1785/BSSA0810062335
- Y. Qian, S. Ni, S. Wei, R. Almeida, H. Zhang, The effects of core-reflected waves on finite fault inversions with teleseismic body wave data. *Geophys. J. Int.* 211, 936– 951 (2017). doi:10.1093/gii/ggx338
- 71. L. Zhu, L. A. Rivera, A note on the dynamic and static displacements from a point source in multilayered media. *Geophys. J. Int.* **148**, 619–627 (2002). doi:10.1046/j.1365-246X.2002.01610.x
- W. Fan, P. M. Shearer, Detailed rupture imaging of the 25 April 2015 Nepal earthquake using teleseismic P waves. *Geophys. Res. Lett.* 42, 5744–5752 (2015). doi:10.1002/2015GL064587
- 73. E. Nissen, J. Elliott, R. Sloan, T. Craig, G. Funning, A. Hutko, B. Parsons, T. Wright, Limitations of rupture forecasting exposed by instantaneously triggered earthquake doublet. *Nat. Geosci.* **9**, 330–336 (2016). doi:10.1038/ngeo2653

First release: 3 August 2023

- 74. D. Wang, N. Takeuchi, H. Kawakatsu, J. Mori, Estimating high frequency energy radiation of large earthquakes by image deconvolution back-projection. *Earth Planet. Sci. Lett.* **449**, 155–163 (2016). doi:10.1016/j.epsl.2016.05.051
- S. P. Hicks, R. Okuwaki, A. Steinberg, C. A. Rychert, N. Harmon, R. E. Abercrombie, P. Bogiatzis, D. Schlaphorst, J. Zahradnik, J.-M. Kendall, Y. Yagi, K. Shimizu, H. Sudhaus, Back-propagating supershear rupture in the 2016 M w 7.1 Romanche transform fault earthquake. *Nat. Geosci.* 13, 647–653 (2020). doi:10.1038/s41561-020-0619-9
- S. Rost, C. Thomas, Array seismology: Methods and applications. *Rev. Geophys.* 40, 21–27 (2002). doi:10.1029/2000RG000100
- 77. Y. Xu, K. D. Koper, O. Sufri, L. Zhu, A. R. Hutko, Rupture imaging of the Mw 7.9 12 May 2008 Wenchuan earthquake from back projection of teleseismic P waves. *Geochem. Geophys. Geosyst.* 10.1029/2008GC002335 (2009). doi:10.1029/2008GC002335
- 78. S. H. Hartzell, T. H. Heaton, Rupture history of the 1984 Morgan Hill, California, earthquake from the inversion of strong motion records. *Bull. Seismol. Soc. Am.* **76**, 649–674 (1986). doi:10.1785/BSSA0760030649
- C. Ji, D. J. Wald, D. V. Helmberger, Source description of the 1999 Hector Mine, California, earthquake, part I: Wavelet domain inversion theory and resolution analysis. *Bull. Seismol. Soc. Am.* 92, 1192–1207 (2002). doi:10.1785/0120000916
- 80. M. Grant, S. Boyd, CVX: Matlab software for disciplined convex programming, version 2.1 (CVX Research, 2014).
- 81. R. A. Harris, M. Barall, D. J. Andrews, B. Duan, S. Ma, E. M. Dunham, A.-A. Gabriel, Y. Kaneko, Y. Kase, B. T. Aagaard, D. D. Oglesby, J.-P. Ampuero, T. C. Hanks, N. Abrahamson, Verifying a computational method for predicting extreme ground motion. *Seismol. Res. Lett.* **82**, 638–644 (2011). doi:10.1785/gssrl.82.5.638
- 82. M. D. Ramos, P. Thakur, Y. Huang, R. A. Harris, K. J. Ryan, Working with dynamic earthquake rupture models: A practical guide. *Seismol. Res. Lett.* **93**, 2096–2110 (2022). doi:10.1785/0220220022
- D. Andrews, Rupture propagation with finite stress in antiplane strain. J. Geophys. Res. 81, 3575–3582 (1976). doi:10.1029/JB081i020p03575
- 84. S. Das, K. Aki, Fault plane with barriers: A versatile earthquake model. *J. Geophys. Res.* **82**, 5658–5670 (1977). doi:10.1029/JB082i036p05658
- 85. E. H. Madden, T. Ulrich, A. A. Gabriel, The State of Pore Fluid Pressure and 3-D Megathrust Earthquake Dynamics. *J. Geophys. Res. Solid Earth* 127, e2021JB023382 (2022). doi:10.1029/2021JB023382
- 86. J. R. Rice, "Fault stress states, pore pressure distributions, and the weakness of the San Andreas fault" in *International geophysics* (Elsevier, 1992), vol. 51, pp. 475-503.
- 87. J. Suppe, Fluid overpressures and strength of the sedimentary upper crust. *J. Struct. Geol.* **69**, 481–492 (2014). doi:10.1016/j.isg.2014.07.009
- 88. S. Wollherr, A. A. Gabriel, P. M. Mai, Landers 1992 "reloaded": Integrative dynamic earthquake rupture modeling. *J. Geophys. Res. Solid Earth* **124**, 6666–6702 (2019). doi:10.1029/2018JB016355
- 89. T. Ulrich, A.-A. Gabriel, E. H. Madden, Stress, rigidity and sediment strength control megathrust earthquake and tsunami dynamics. *Nat. Geosci.* **15**, 67–73 (2022). doi:10.1038/s41561-021-00863-5
- J. R. Weiss, R. J. Walters, Y. Morishita, T. J. Wright, M. Lazecky, H. Wang, E. Hussain, A. J. Hooper, J. R. Elliott, C. Rollins, C. Yu, P. J. González, K. Spaans, Z. Li, B. Parsons, High-resolution surface velocities and strain for Anatolia from Sentinel-1 InSAR and GNSS data. *Geophys. Res. Lett.* 47, e2020GL087376 (2020). doi:10.1029/2020GL087376
- S. Peyrat, K. Olsen, Nonlinear dynamic rupture inversion of the 2000 Western Tottori, Japan, earthquake. *Geophys. Res. Lett.* 10.1029/2003GL019058 (2004). doi:10.1029/2003GL019058
- 92. F. Gallovič, L. Valentová, J. P. Ampuero, A. A. Gabriel, Bayesian dynamic finite-fault inversion: 1. Method and synthetic test. *J. Geophys. Res. Solid Earth* **124**, 6949–6969 (2019). doi:10.1029/2019JB017510
- E. Tinti, P. Spudich, M. Cocco, Earthquake fracture energy inferred from kinematic rupture models on extended faults. *J. Geophys. Res. Solid Earth* 110, JB003644 (2005).
- 94. H. Weng, H. Yang, Constraining frictional properties on fault by dynamic rupture simulations and near-field observations. *J. Geophys. Res. Solid Earth* **123**, 6658–6670 (2018). doi:10.1029/2017.JB015414

- 95. A. M. Rubin, J. P. Ampuero, Earthquake nucleation on (aging) rate and state faults. J. Geophys. Res. Solid Earth 110, JB003686 (2005).
- 96. R. A. Harris, M. Barall, B. Aagaard, S. Ma, D. Roten, K. Olsen, B. Duan, D. Liu, B. Luo, K. Bai, J.-P. Ampuero, Y. Kaneko, A.-A. Gabriel, K. Duru, T. Ulrich, S. Wollherr, Z. Shi, E. Dunham, S. Bydlon, Z. Zhang, X. Chen, S. N. Somala, C. Pelties, J. Tago, V. M. Cruz-Atienza, J. Kozdon, E. Daub, K. Aslam, Y. Kase, K. Withers, L. Dalguer, A suite of exercises for verifying dynamic earthquake rupture codes. Seismol. Res. Lett. 89, 1146-1162 (2018). doi:10.1785/0220170222
- 97. S. Wollherr, A.-A. Gabriel, C. Uphoff, Off-fault plasticity in three-dimensional dynamic rupture simulations using a modal Discontinuous Galerkin method on unstructured meshes: Implementation, verification and application. Geophys. J. Int. 214, 1556-1584 (2018). doi:10.1093/gji/ggy213
- 98. D. Roten, K. Olsen, S. Day, Y. Cui, D. Fäh, Expected seismic shaking in Los Angeles reduced by San Andreas fault zone plasticity. Geophys. Res. Lett. 41, 2769-2777 (2014). doi:10.1002/2014GL059411
- 99. M. Dumbser, M. Käser, An arbitrary high-order discontinuous Galerkin method for elastic waves on unstructured meshes—II. The three-dimensional isotropic case. Geophys. J. Int. 167, 319-336 (2006). doi:10.1111/j.1365-246X.2006.03120.x
- 100. A. Heinecke, A. Breuer, S. Rettenberger, M. Bader, A.-A. Gabriel, C. Pelties, A. Bode, W. Barth, X.-K. Liao, K. Vaidyanathan, in SC'14: Proceedings of the International Conference for High Performance Computing, Networking, Storage and Analysis. (IEEE, 2014), pp. 3-14.
- 101. S. Rettenberger, O. Meister, M. Bader, A.-A. Gabriel, in Proceedings of the Exascale Applications and Software Conference 2016. (2016), pp. 1-9.
- 102. C. Uphoff, S. Rettenberger, M. Bader, E. H. Madden, T. Ulrich, S. Wollherr, A.-A. Gabriel, in Proceedings of the international conference for high performance computing, networking, storage and analysis. (2017), pp. 1-16.
- 103. C. Pelties, A.-A. Gabriel, J.-P. Ampuero, Verification of an ADER-DG method for complex dynamic rupture problems. Geosci. Model Dev. 7, 847-866 (2014). doi:10.5194/gmd-7-847-2014
- 104. D. Andrews, Rupture models with dynamically determined breakdown 769-775 displacement. Bull. Seismol. Soc. Am. 94, (2004).doi:10.1785/0120030142
- 105. Y. A. Fialko, A. M. Rubin, What controls the along-strike slopes of volcanic rift zones? J. Geophys. 104 (B9), 20007-20020 Res. doi:10.1029/1999JB900143
- 106. L. L. Erickson, "A three-dimensional dislocation program with applications to faulting in the earth", thesis, Stanford University (1986).
- 107. D. M. Boore, J. Watson-Lamprey, N. A. Abrahamson, Orientation-independent measures of ground motion. Bull. Seismol. Soc. Am. 96 (4A), 1502-1511 (2006). doi:10.1785/0120050209
- 108. W. B. Joyner, D. M. Boore, Peak horizontal acceleration and velocity from strongmotion records including records from the 1979 Imperial Valley, California, earthquake Bull. Seismol. Soc. Am. 71, 2011–2038 doi:10.1785/BSSA0710062011
- 109. D. J. Wald, B. C. Worden, V. Quitoriano, K. L. Pankow, "ShakeMap manual: technical manual, user's guide, and software guide" (2005).
- 110. M. Pagani, D. Monelli, G. Weatherill, L. Danciu, H. Crowley, V. Silva, P. Henshaw, L. Butler, M. Nastasi, L. Panzeri, M. Simionato, D. Vigano, OpenQuake engine: An open hazard (and risk) software for the global earthquake model. Seismol. Res. Lett. 85, 692-702 (2014). doi:10.1785/0220130087
- 111. T. M. Brocher, Empirical relations between elastic wavespeeds and density in the Earth's crust. Bull. Seismol. Soc. Am. 95, 2081-2092 (2005). doi:10.1785/0120050077

ACKNOWLEDGMENTS

First release: 3 August 2023

We thank constructive comments by the editor Brent Grocholski and two anonymous reviewers. The facilities of IRIS Data Services, and specifically the IRIS Data Management Center, were used for access to waveforms, related metadata, and/or derived products used in this study. The GNSS data are provided by the General Directorate of Land Registry and Cadastre, and the General Directorate of Mapping, Turkey. IRIS Data Services are funded through the Seismological Facilities for the Advancement of Geoscience (SAGE) Award of the National Science Foundation under Cooperative Support Agreement EAR-1851048. We thank the Engineering Strong-Motion (ESM) Database by ORFEUS

(52) for providing access to the data from the Turkish National Strong Motion Network, which is operated by Turkey's Disaster and Emergency Management Authority (AFAD). The computations in this study were supported by the supercomputer SuperMUC-NG. Funding: Funding for this work was provided by the National Science Foundation (EAR-2123529, EAR-1841273 to Y.F., EAR-2022441, EAR-2143413 to W.F., EAR-2121666 to A.A.G), the National Aeronautics and Space Administration (80NSSC22K0506 to Y.F., 80NSSC20K0495 to A.A.G.), the United States Geological Survey (G22AP00011 to P.S. and W.F.), and the Cecil and Ida Green Foundation. M.M., T.U. and A.A.G. were supported by the European Union's Horizon 2020 Research and Innovation Programme (TEAR grant No. 852992) and Horizon Europe (ChEESE-2P grant No. 101093038, DT-GEO grant No. 101058129 and Geo-INQUIRE grant No.101058518). J.R. was supported by the National Science Foundation Graduate Research Fellowship Program (grant No. DGE-2038238). A.A.G. gratefully acknowledges the Gauss Centre for Supercomputing e.V. (www.gausscentre.eu) for providing computing time on the GCS Supercomputer SuperMUC-NG at Leibniz Supercomputing Centre (www.lrz.de), in project pn49ha. Author contributions: Z.Jia led the study, performed the subevent and kinematic slip inversions, and wrote the initial draft of the manuscript. Z.Jin, X.Z., and Y.F. processed the InSAR data, quantified the fault geometry, and performed static slip inversion. M.M., T.U., and A.A.G. performed the dynamic rupture simulations and the Coulomb failure stress analysis. W.F. performed back projection analysis and coordinated the collaboration. Y.F. conducted static Coulomb stress calculations. X.Z. contributed to the fault geometry determination and figure design. J.R., T.U., and A.A.G. conducted the ground motion analysis. F.B. and A.G. processed the GNSS data. W.F., P.S., A.A.G., Y.F. supervised the modeling and contributed to interpretation of the results. A.A.G., Y.F., and W.F. provided access to computational resources. All authors discussed the results and contributed to writing and revising the manuscript. Competing interests: Authors declare no competing interests. **Data and materials availability**: The Sentinel-1 SAR data are provided by the European Space Agency (ESA) and mirrored at the Alaska SAR Facility (ASF). The ALOS-2 PALSAR data are owned by the Japanese Space Agency (JAXA) and provided to Y.F. under a Research User Agreement. The global seismic data are publicly available from the IRIS-DMC. The regional strong motion data are publicly available from the EMS Database by ORFEUS. The geodetic and seismic data, the data-driven slip models and subevent models, and the data required to reproduce the dynamic rupture earthquake sequence scenarios can be downloaded from https://doi.org/10.5281/zenodo.8128343. We provide detailed README files summarizing the data and data formats provided. License information: Copyright © 2023 the authors, some rights reserved; exclusive licensee American Association for the Advancement of Science. No claim to original US government works. https://www.science.org/about/science-licenses-journalarticle-reuse

SUPPLEMENTARY MATERIALS

science.org/doi/10.1126/science.adi0685 Materials and Methods Figs. S1 to S28 Tables S1 and S2 References (56-111) Movies S1 to S3

Submitted 1 April 2023; accepted 19 July 2023 Published online 3 August 2023 10.1126/science.adi0685

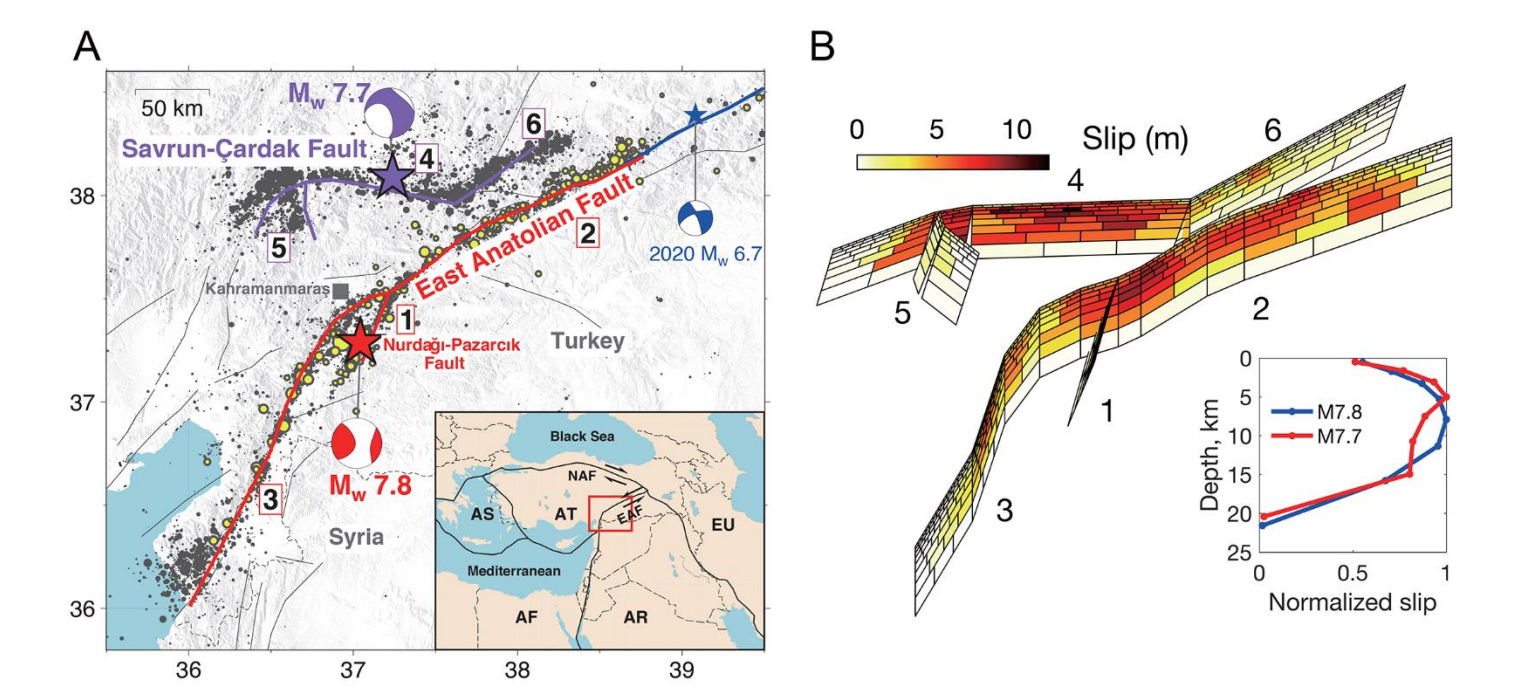


Fig. 1. A multi-fault earthquake doublet. (A) Tectonic background and aftershock seismicity of the study area near Kahramanmaraş, Turkey. Red and purple stars indicate the $M_{\rm w}$ 7.8 and 7.7 earthquake epicenters from the Turkey Disaster and Emergency Management Authority (53), and beachballs show focal mechanisms from the Global Centroid Moment Tensor catalog, respectively. Red and purple lines show surface ruptures identified from SAR data (26). Yellow dots show aftershocks for the period between the $M_{\rm w}$ 7.8 and 7.7 earthquakes and black dots are aftershocks following the $M_{\rm w}$ 7.7 event (28). The blue line and beachball denote the rupture extent and focal mechanism of the 2020 $M_{\rm w}$ 6.7 Elazig earthquake (29). Inset shows the regional tectonics and major plate boundary faults (solid black lines). Red outline denotes the study area. (B) Finite-fault model of the 2023 doublet derived from inversions of space geodetic (InSAR and GNSS) data. Fault segment numbers correspond to those shown in panel (A), in order of their rupture time: 1 - Nurdağı-Pazarcık Fault, 2 and 3 - East Anatolian Fault, 4-6 - Savrun-Çardak Fault. The inset panel shows the along-strike averaged coseismic slip normalized by the maximum slip amplitude, as a function of depth (49).

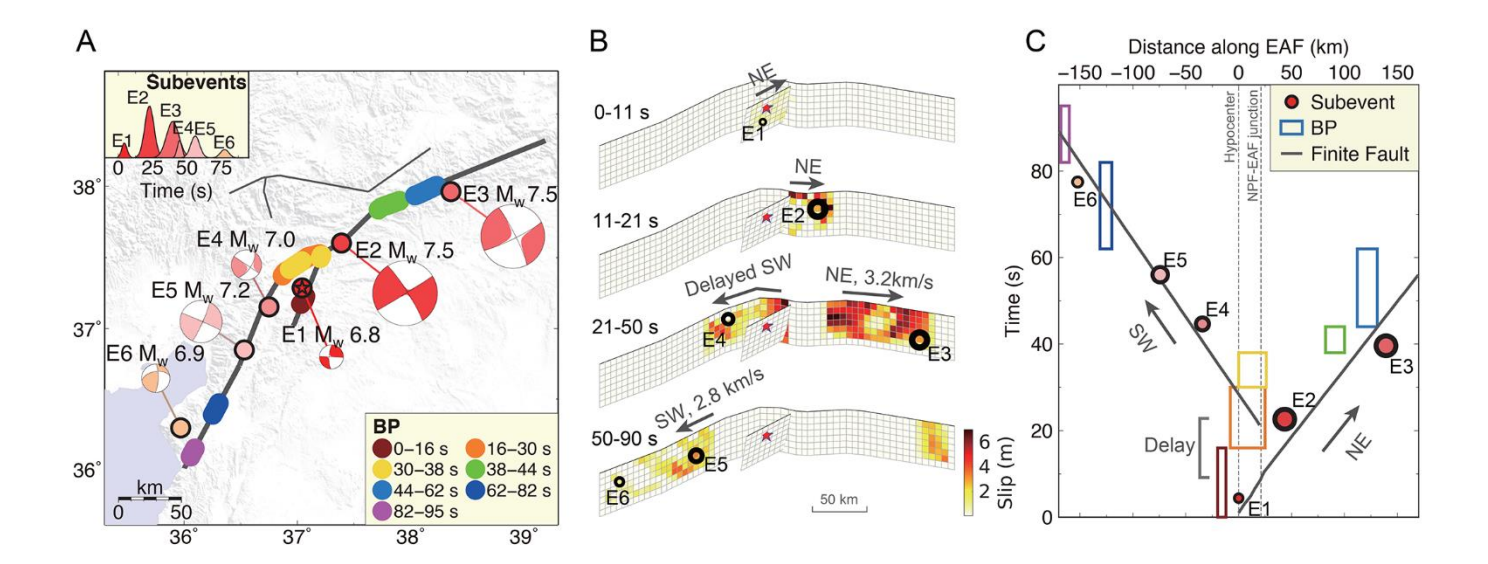


Fig. 2. Complex slip evolution of the $M_{\rm w}$ 7.8 earthquake, including delayed initiation of slip. (A) Subevent model from near- and far-field seismic observations and back-projection results, suggesting that the $M_{\rm w}$ 7.8 earthquake initiated on the NPF-1 (fault 1 in Fig. 1B), then propagated bilaterally, NE along the EAF-2 (fault 2) and SW along the EAF-3 (fault 3). The rupture of fault 2 terminates around 50 s, while rupture of fault 3 continues for an additional 30 s. (B) Rupture history within different time intervals from our kinematic slip inversion of far-and near-field seismic and geodetic data. We infer rupture velocities of 3.2 and 2.8 km/s for the NE and SW episodes, respectively, and a 10 s delay in the onset of the SW rupture along EAF-3 with respect to the NE rupture along EAF-2. The slip distribution within each time interval agrees with the subevent (black circles) inversion. (C) Subevents, back-projection locations and times, and finite-fault velocities (in B) consistently indicate delayed initiation of slip on branch EAF-3.

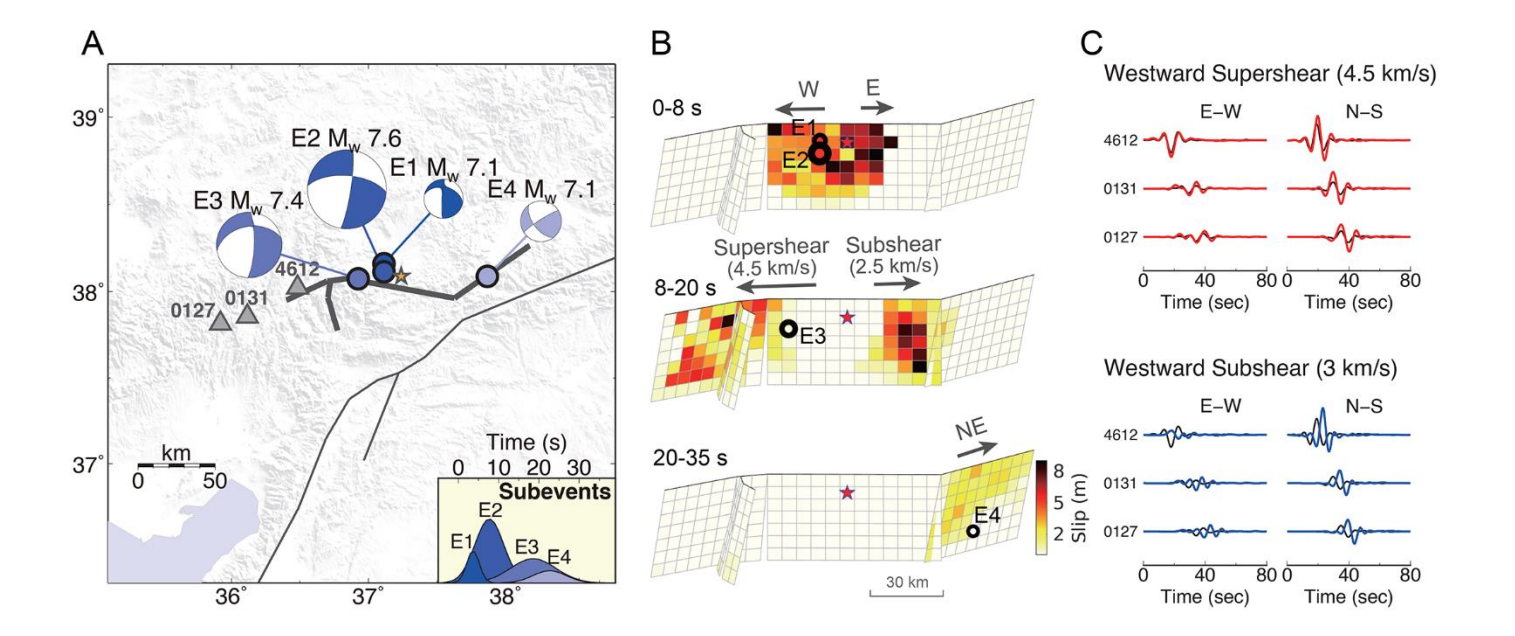


Fig. 3. Asymmetric kinematics of the M_w 7.7 earthquake. (A) Three subevents close to the hypocenter suggest a bilateral rupture. The fourth event images the rupture of the Doğanşehir branch (fault 6 in Fig. 1B). (B) Asymmetric bilateral rupture velocities of the $M_{\rm w}$ 7.7 event. The westward rupture has an inferred supershear velocity of 4.5 km/s, whereas a subshear velocity is seen toward the east (2.5 km/s). Note that subevent locations are based on their seismic moment centroids. The slip may not be the largest at the centroid location, specifically for bilateral ruptures. For example, E3 (10-30 s) averages slip pulses of both the westward supershear and the eastward subshear rupture. (C) A westward supershear rupture velocity (red waveforms) better explains observed waveforms (black) at near-fault strong motion stations to the west (triangles in A) than a subshear rupture (blue).

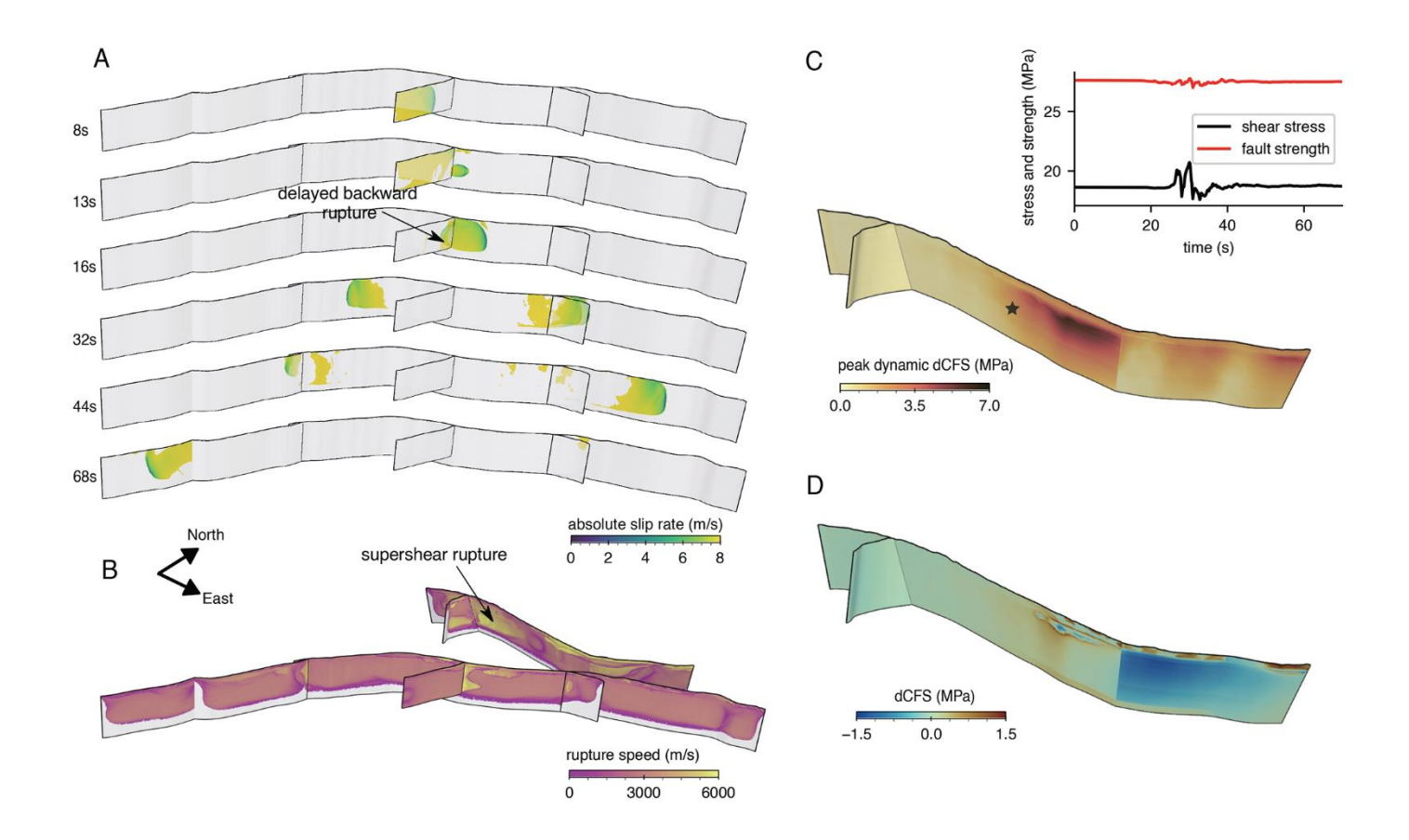


Fig. 4. 3D dynamic rupture scenarios and stress-mediated interactions of the $M_{\rm w}$ 7.8 and 7.7 earthquakes. (A) Snapshots of absolute slip rate evolution in the $M_{\rm w}$ 7.8 dynamic rupture scenario (movie S1). (B) Modeled rupture speeds in linked dynamic rupture simulations (54) of both earthquakes indicating dominantly subshear rupture speeds but sustained westward supershear during the $M_{\rm w}$ 7.7 scenario (fig. S21 and movie S2). (C) Peak absolute dynamic shear stress perturbation reaching up to 7 MPa measured in the direction of maximum initial traction. Inset: Evolution of dynamic shear stress and fault strength at the M_w 7.7 hypocenter (black star). (D) Static Coulomb failure stress changes ΔCFS assuming a static friction coefficient of 0.6.

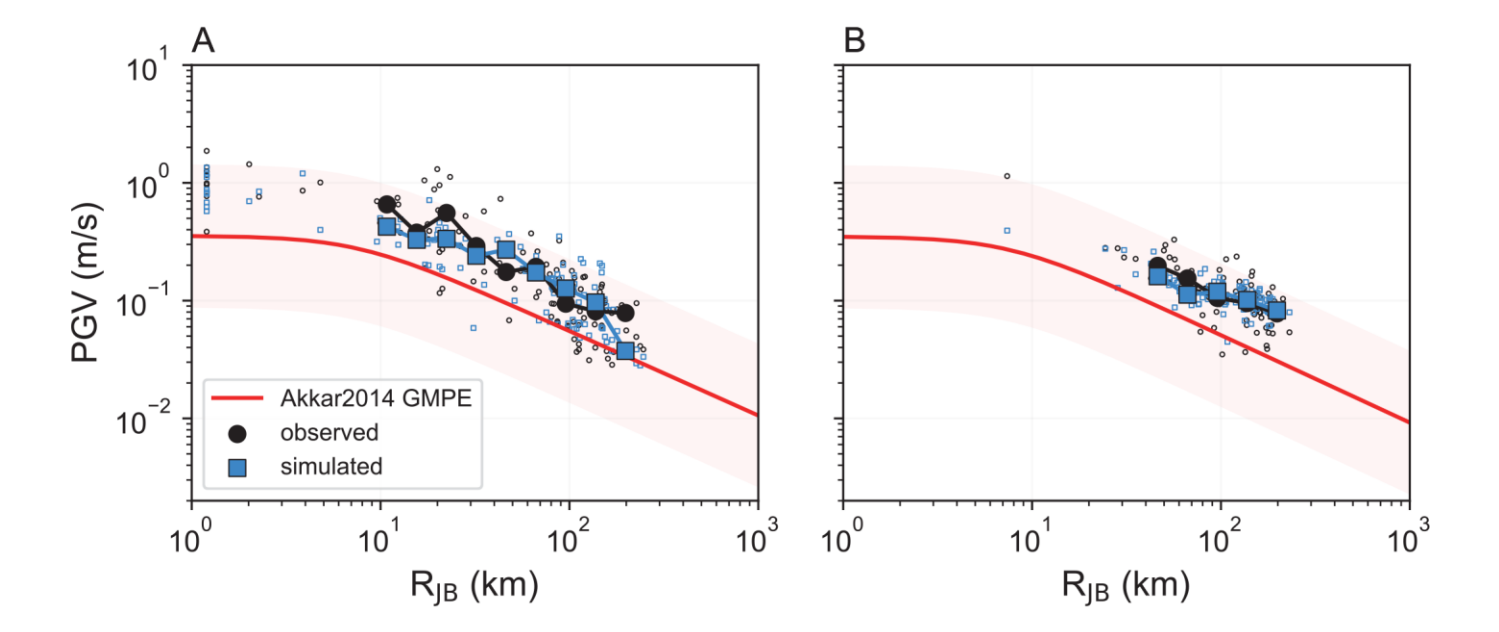


Fig. 5. Peak ground velocities (PGV) plotted against Joyner-Boore distance (R_{JB}) for the M_{W} 7.8 (A) and M_{W} 7.7 (B) earthquakes. Observed PGVs from strong motion accelerometers are indicated by open black circles, and simulated PGVs from the dynamic rupture simulations are indicated by open blue squares. We bin the PGV data by R_{JB} and plot the medians for each distance bin (solid markers). The red curve indicates PGV predicted by a ground motion model (55) assuming an average shear wave velocity for the top 30 m of soil (VS_{30}) of 760 m/s, with the shaded area denoting its uncertainty. All PGV are rotationally independent geometric mean values (GMRotD50). We include simulated and observed data at the same locations, respectively.



The complex dynamics of the 2023 Kahramanmara#, Turkey, $M_{\rm W}$ 7.8-7.7 earthquake doublet

Zhe Jia, Zeyu Jin, Mathilde Marchandon, Thomas Ulrich, Alice-Agnes Gabriel, Wenyuan Fan, Peter Shearer, Xiaoyu Zou, John Rekoske, Fatih Bulut, Asli Garagon, and Yuri Fialko

Science, Ahead of Print DOI: 10.1126/science.adi0685

View the article online

https://www.science.org/doi/10.1126/science.adi0685

Permissions

https://www.science.org/help/reprints-and-permissions

Use of this article is subject to the Terms of service